Article

Relationship between Rock Porosity and Infrared Cooling Rate in Non-Standard Specimens of Tuffs Used in the Hungarian Cultural Heritage

Simone Mineo [1], Luigi Germinario [2,3], Ákos Török [3] and Giovanna Pappalardo [1,*]

[1] Department of Biological, Geological and Environmental Sciences, University of Catania, Corso Italia 57, 95129 Catania, Italy; simone.mineo@unict.it
[2] Department of Geosciences, University of Padova, Via Gradenigo 6, 35131 Padova, Italy; luigi.germinario@gmail.com
[3] Department of Engineering Geology and Geotechnics, Budapest University of Technology and Economics, Műegyetem rkp. 3, 1111 Budapest, Hungary; torok.akos@emk.bme.hu
* Correspondence: giovanna.pappalardo@unict.it

Abstract: This paper is focused on the application of Infrared Thermography to non-standard rock specimens, in terms of size and deterioration conditions, of Hungarian tuff to monitor their cooling process and to look for a relationship between the rock Cooling Rate Index and the porosity. Literature data agree on the potential of Infrared Thermography for the indirect estimation of rock porosity in fresh specimens through the IRTest, but this technique has never been tested on non-standard specimens. To this purpose, tests on three varieties of Hungarian tuffs were carried out. These materials were selected for their cultural importance linked to their usage as building stones and in other historical applications in Northern Hungary. Tuff specimens underwent a fixed number of salt crystallization cycles. The Cooling Rate Index (CRI) for each specimen was calculated according to the literature experience and correlated to their porosity estimated by water, helium, and mercury intrusion. The results show that the rock cooling process is related to porosity since more porous rocks are characterized by faster cooling. Positive linear trends were achieved for weathered specimens considering 20 min monitoring (CRI_{20}), which is double the time suitable for untreated rocks. The reason should be searched in salt crystallization's effects on the rock texture, paving the way to further studies on this pioneering branch of technological application.

Keywords: Cooling Rate Index; intact rock specimen; porosity; weathering; tuff

1. Introduction

Porosity is a physical property conditioning rock mechanical behavior under stress in terms of strength and deformability [1–5]. The presence of a void network within the rock represents a weakening feature, reducing the contact between grains, lowering rock resistance against axial stresses, and enhancing the rock attitude towards deformation. The solid literature experience in this subject points out that Uniaxial Compressive Strength (UCS) and Young's modulus are inversely proportional to porosity, with statistical trends scattered depending also on the type of voids in the rock, i.e., pores or cracks or both, e.g., [6–8]. Porosity is recognized to be also related to rock durability from the point of view of weathering. In fact, the growth of salt and ice crystals in the pore system and their related stresses can be acknowledged among the major deterioration mechanisms of porous materials [9–15]. This physical property can be referred to as "effective" and "total" depending on whether only the volume of interconnected voids or the total void volume, respectively, is considered. Porosity estimation is therefore relevant for predicting the behavior of rocks used as construction or building materials and specific engineering geological aspects. The International Society for Rock Mechanics (ISRM) and the European Committee for Standardization Comité Européen de Normalisation (CEN) defined

the standard procedures to estimate such properties on intact rock specimens following different steps, such as saturation, rock volume estimation, and the pycnometer analysis on a pulverized specimen fraction [16,17]. With respect to the effective porosity, the results achieved by such procedures refer to the pore volume that can be filled with water, and this kind of porosity will be defined from now on in the text, as n'_{H_2O}. Other approaches are based on the use of gases (helium, nitrogen, carbon dioxide, etc.) or liquids (mercury), which are forced to fill the rock voids under a pressure gradient for the porosity estimation (e.g., n_{He} and n'_{Hg}). In any case, these operations require rock specimen destruction to prepare either a powder or a small rock fragment. Still, other techniques are based on microscopic image analysis, but their measurement range and accuracy are relatively limited and may still require sample preparation for best results [18]. In the last decade, an innovative procedure for the non-destructive estimation of rock porosity through Infrared Thermography (IRT) was presented [19–22]. The IRTest is based on the positive correlation existing between the cooling rate of an oven-heated rock specimen and its porosity, representing a promising quick experimental procedure. In the literature, IRTests have been performed on regularly shaped intact rock specimens, sized according to international standards, to estimate both total porosity and n'_{H_2O}, proving that the cooling rate within the first 10 min of monitoring (CRI_{10}) is a promising index for the indirect prediction of such physical property. Nevertheless, the IRTest has never been tested on non-standard specimens in terms of size and deterioration conditions. In this perspective, the aim of this paper is to find out whether this can provide information on the rock porosity of small rock specimens, even after artificial aging by salt crystallization cycles. These experimental requirements may reflect, among other things, those for testing historical materials in cultural heritage, which often entail restricted sampling and a bad state of conservation. To this purpose, tests on three varieties of Hungarian tuffs were carried out. These materials were selected for their cultural importance linked to their usage as medieval building stones and in other historical applications, especially in the region of Northern Hungary. Tuff specimens were grouped into six groups, each undergoing a fixed number of salt crystallization cycles. For each specimen, the Cooling Rate Index (CRI) was calculated according to the literature experience, and then porosity was estimated under water, helium, and/or mercury intrusion. The data collected were finally used for statistical correlations to shed light on the suitability of the IRTest for the porosity assessment of non-standard rock specimens.

2. Materials

The materials investigated herein are pyroclastic rocks historically used as building and ornamental stones in Hungary, named after the towns of Bogács, Demjén, and Sirok in the Eger region (Northern Hungary), where they are quarried. These tuffs have a centuries-old tradition of usage that commenced as early as the Middle Ages. Remarkable examples of historical monuments made of tuff include Christian fortifications and churches, for instance, the 13th-century castle and the 19th-century Baroque cathedral of Eger, as well as Ottoman mosques and baths (17th century) (Figure 1). These stones have also had more modest, although widespread, applications in vernacular architecture, for building houses, cave dwellings, wine cellars, burials, etc. [23,24].

Considering their geological background, they belong to a sequence of Miocene welded and unwelded pumiceous tuffs with a prevailing high-K rhyolitic composition, formed between 18.2 and 14.4 Ma during the tectonic evolution of the Carpathian-Pannonian Region [25]. They are classifiable as pumice tuffs with a pseudo-porphyritic texture, glassy groundmass, and a mineralogical assemblage composed mainly of plagioclase, biotite, quartz, and occasionally, amphibole and pyroxene; swelling clay minerals are the most significant secondary phases.

Demjén tuff is the most porous and soft, with compressive and tensile strengths of 10 and 1 MPa, respectively. Bogács and Sirok tuffs have better physical and mechanical properties, with compressive strength and tensile strength in the ranges of 26–28 MPa and

3–4 MPa. For all three tuff varieties, water saturation may cause an extreme deterioration of the mechanical performance [23].

Figure 1. Examples of the historical usage of tuffs in the town of Eger: the Medieval castle and the Ottoman minaret. The insets show the location of the study quarry sites (a few kilometers apart) and the macroscopic appearance of Demjén tuff used in the monuments.

3. Methods

The methodological approach set for this study can be summarized by 4 main points: (1) salt crystallization tests; (2) IRTest for the calculation of the Cooling Rate Indexes; (3) rock porosity estimation under water, helium, and mercury intrusion; (4) statistical data processing.

3.1. Salt Crystallization Tests

Salt crystallization tests were performed to reproduce the rock degradation effects naturally arising from the weathering phenomena involving in-pore water circulation. Tuff specimens had a non-standard shape, being cylinders with a 50 mm diameter and a 30 mm height. A total of 72 specimens were prepared. These were then grouped into 6 sets, each undergoing a different number of crystallization cycles (0, 2, 4, 6, 10, 23), with 1 set serving as an untreated reference (Cycle 0). The different steps were chosen based on how quickly the observed state of conservation changed, so as to isolate representative samples for different decay stages for the following IRTests. According to the standard test method EN 12370 (1999), each salt crystallization cycle consisted of the following phases: 2 h total immersion in a 14% Na_2SO_4 aqueous solution, minimum 16 h drying at 105 °C, and 2 h cooling. After each cycle, the sample mass and macroscopic changes were recorded.

3.2. Infrared Cooling Monitoring and CRI Calculation

The IRT technique relies on the principle that every material at a temperature above absolute zero emits thermal radiation. This is characterized by a wavelength mainly falling within the infrared band of the electromagnetic spectrum [26], and it is proportional to the temperature of the emitting body, according to the Stefan–Boltzmann law. Therefore, the surface temperature of a body can be easily estimated by a thermal camera, which is a device operating within the range of wavelengths as long as 13–14 μm. The use of IRT for rock characterization has increasingly become the subject of numerous scientific studies focused either on rock deterioration and fracturing state [11,27–30] or on rocky outcrops [31–36].

Recent literature studies shed light on the positive correlation between rock cooling, monitored by IRT, and porosity [19–22]. Starting from the hypothesis that the presence of voids within the rock texture could affect its thermal behavior, a series of tests on numerous intact rock specimens were performed. These proved that the greater the porosity of the rock, the faster its cooling is.

The IRTest on intact rock specimens is carried out according to the following four main stages:

(1) Oven-heating of the rock specimens for 24 h at 70 $\pm$ 5 °C.

(2) Monitoring of the rock cooling by acquiring regular IRT images of the upper face of the specimens, which are placed on a smooth laminate worktop in a temperature-controlled room (25 $\pm$ 1 °C), for a defined time interval. The initial IRT frame is acquired when the cooling begins, thus representing the reference for the following stage.

(3) Post-processing of the IRT images in order to define the average surface temperature of the framed specimen face; this is the average temperature value calculated within a specific area of the IR image, set to coincide with the specimen's upper face.

(4) According to Equation (1), the Cooling Rate Index (CRI) of the rock is calculated for a defined monitoring time window. CRI is expressed by the ratio between the difference of temperature between two measurements (ΔT) within a specific time window (Δt).

$$CRI = \Delta T / \Delta t \tag{1}$$

Literature outcomes agree that the best relationship between rock porosity (estimated by buoyancy in water) and rock cooling is achieved by calculating the CRI within a 10 min time window starting from when the cooling begins (CRI_{10}). A satisfactory correlation was found for rocks belonging to different geological formations and for different shapes and sizes of specimens [19–22].

In this paper, the IRTest was experimentally carried out, on the same specimens prepared for salt crystallization (see Section 3.1), by using a high-sensitivity infrared thermal imaging camera with a 320 $\times$ 240 pixels infrared resolution and operating in a range of temperatures from -20 to 650 °C (with ± 2 °C accuracy) and a thermal sensitivity < 0.04 °C. The rock emissivity was set to 0.975, suitable for the rock type tested according to the literature [37].

Rock IR monitoring had a 5 min cadence, thus allowing the final computation of CRI within the first 5, 10, 15, and 20 min from the cooling beginning.

Thermal images were post-processed through software capable of handling radiometric images and extracting the average surface temperature values corresponding to the framed rock specimen face (Figure 2).

3.3. Rock Porosity Estimation

The porosity of the reference group of tuff specimens (Cycle 0) was estimated according to EN1936:2006 by the long-established Archimedes buoyancy method on 16 specimens. This method relies on the measure of three parameters of a single specimen: the weight of the dry specimen (w_d); the weight in air of the specimen fully saturated with water (w_s); and the weight of the saturated specimen suspended and fully immersed in water (the Archimedes weight w_h) [38]. From these weights, and after determining the real rock density (ρ_r) through the pycnometer method, total (n) and effective (n'_{H_2O}) porosities can be calculated according to Equations (2) and (3), where ρ_b is the bulk density.

$$n = \left(1 - \frac{\rho_b}{\rho_r}\right)100 \tag{2}$$

$$n'_{H_2O} = \frac{w_s - w_d}{w_s - w_h} \tag{3}$$
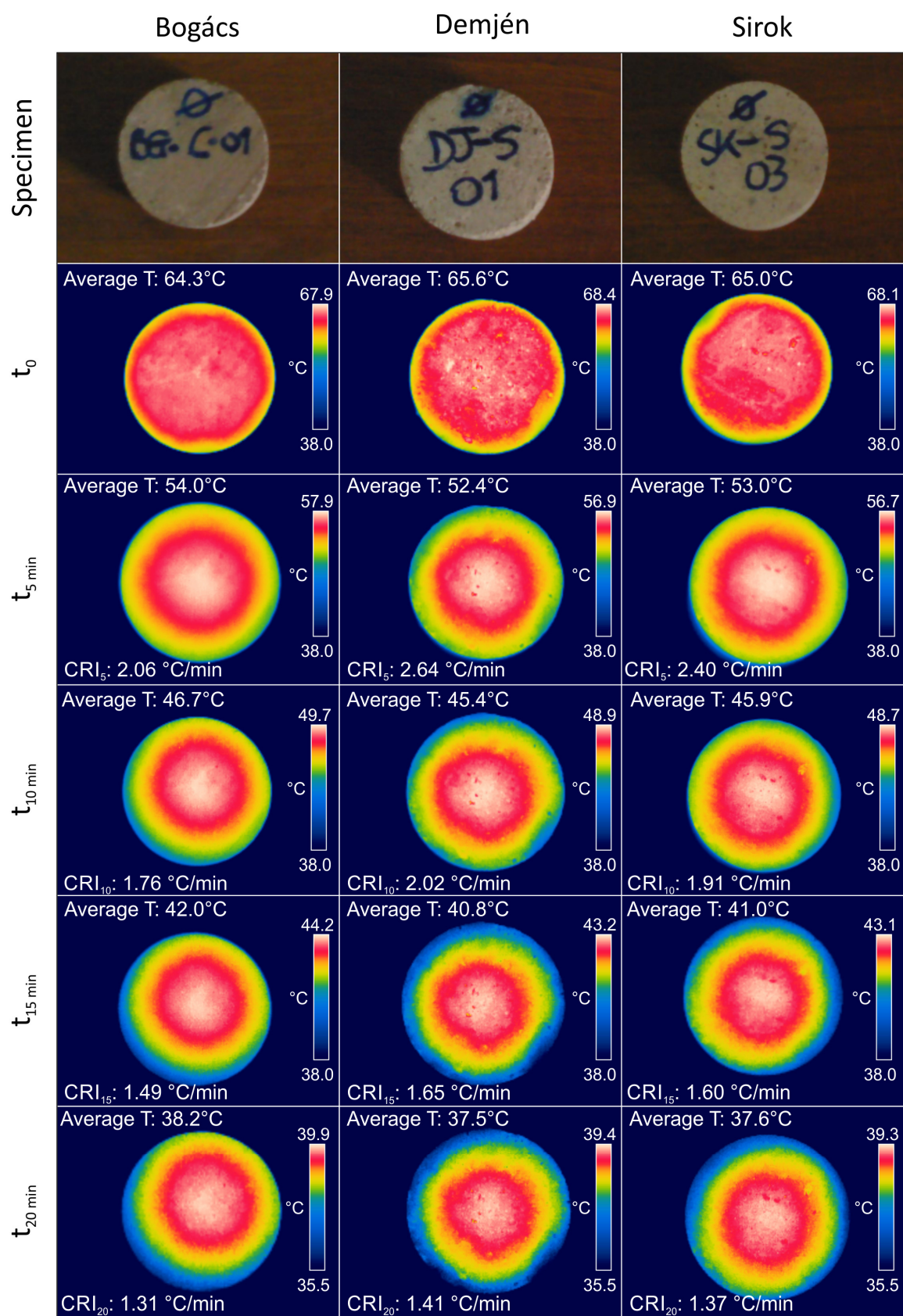
Figure 2. Summary of the IR monitoring for selected representative specimens of each untreated tuff variety.

Some specimens started showing a loose structure from the second cycle, sometimes crumbly even to the touch for the most advanced cycles. This made them unsuitable for saturation with water. Therefore, to avoid errors in the porosity estimation due to both possible salt crystal dissolution and partial loss of specimen mass, porosity was computed by a multianalytical approach using structured-light 3D scanning, helium pycnometry, and mercury intrusion porosimetry (MIP) on 10 representative weathered samples from Cycles 2, 4, 6, 10, and 23.

By structured-light 3D scanning, a Scan-in-a-box FX scanner was combined with the software IDEA 1.1 SR 8 FX for building 3D digital models of the samples and calculating their volume, averaging from three independent measurements. The weighing of the samples provided their bulk density.

By helium pycnometry, a Quantachrome Pentapyc 5200e PPY-30T pycnometer was operated at 25 °C constant temperature and 131 kPa maximum pressure for determining the matrix volume and, indirectly, the matrix density of the samples, averaged among three measurements. Total porosity and pore volume were also calculated.

By MIP, a Quantachrome Poremaster 60 GT porosimeter was used at low pressure (1.5–350 kPa, for pore-throat diameters of 382–4.26 μm) and high pressure (140 kPa–420 MPa, for pore-throat diameters of 10.66–0.004 μm), with two repeated measurements per pressure stage, for determining open porosity, pore-size distribution, and specific surface area.

3.4. Statistical Data Processing

CRIs within 5, 10, 15, and 20 min of cooling were plotted against the n and n'_{H_2O} values for the untreated specimens, measured according to the EN1936:2006 specifications. A simple regression analysis was carried out, and the best-fit curves and the coefficients of determination (R^2) were calculated by the "least squares" method to determine if the correlation between porosity and CRI could be ensured. The achieved statistical trends were then compared to the literature trends [21], referring to specimens similar in shape and size to those tested herein, to prove the reliability of the testing principle. For the other tuff groups (from Cycle 2), CRIs were correlated to n_{He} and n'_{Hg} porosity to find out if significant correlations can be achieved as well.

4. Results of Salt Crystallization Tests

A summary of the results of the salt crystallization tests is shown in Figure 3.

Demjén tuff has the lowest durability to salt crystallization, crumbling already during the first aging cycles. Differential erosion is the main weathering pattern, highlighting the faster disintegration of the groundmass, compared to the slower detachment of the coarser-size phenocrysts.

The resistance of Bogács and Sirok tuffs is distinctively higher instead. Most specimens show negligible macroscopic changes and mass variations (excluding the weight increases due to the continuous salt loading) throughout the experimental program. Bogács tuffs record just the formation of a few voids on the surface and a slight, occasional peeling, which becomes more evident during the very last cycles. On the other hand, several specimens of Sirok tuff start deteriorating after the 5th cycle, with traces of differential erosion, disintegration, and microcracking, leading to mass decreases up to ~10%. These become even clearer during the following cycles, reaching drops of ~25%–30% for some specimens at the end of the tests. The strength variability observed in Sirok tuffs, dependent on changing textural characteristics (e.g., different amounts of pumice clasts, glassy groundmass, coarse phenocrysts and lithoclasts, welding degree), is in agreement with previous experimental observations [23].
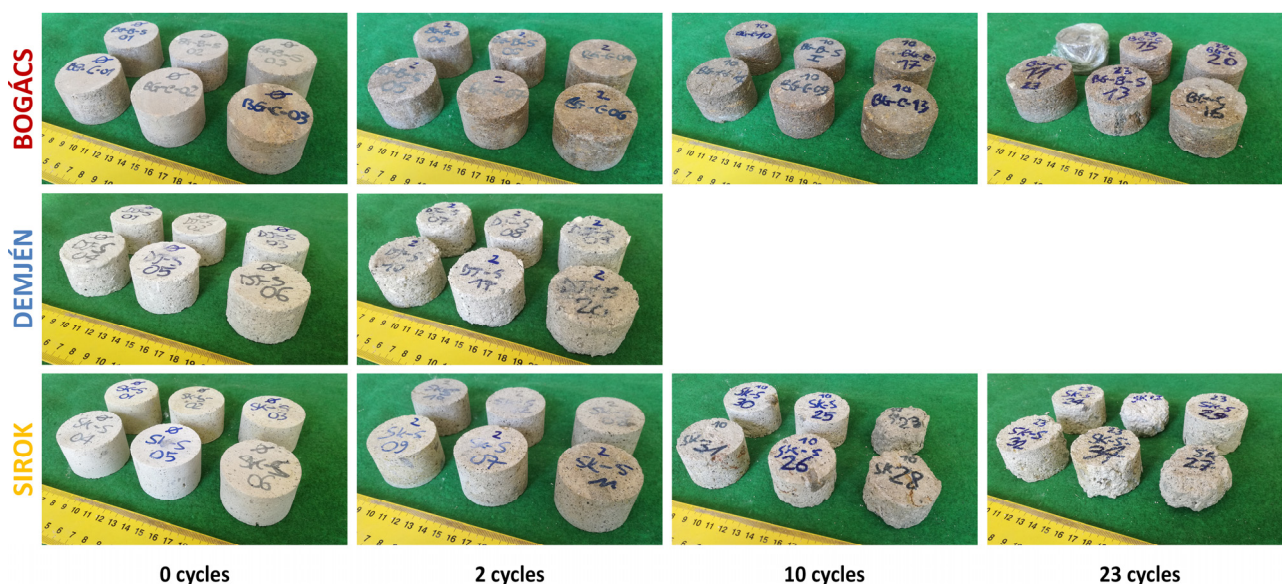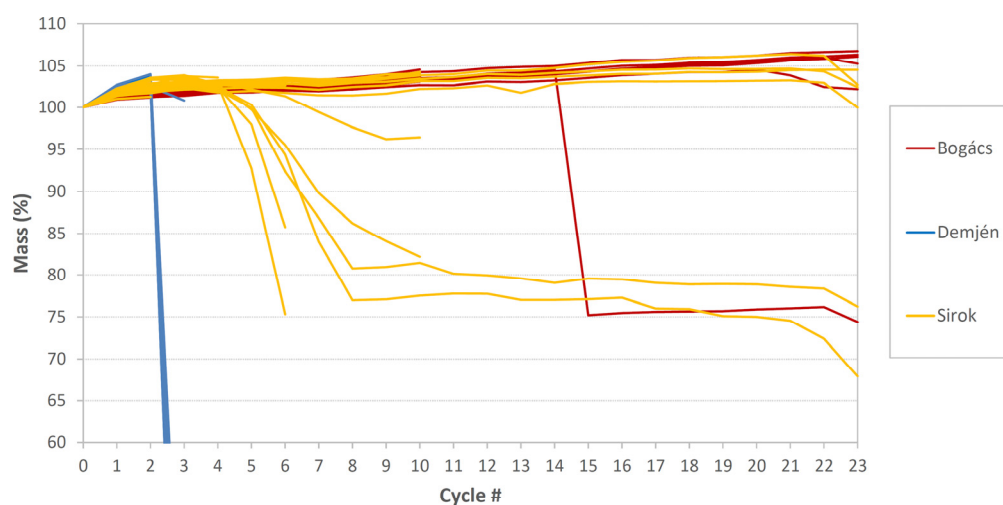
Figure 3. Mass changes of the three tuff varieties during the salt crystallization tests, with photographs of the specimens after different cycles, showing the weathering evolution (the curves refer to all the tested specimens).

5. Results of Porosity Estimation

The initial rock physical characterization, carried out through the method of Archimedes buoyancy in water, returned dissimilar porosity characteristics among the tested tuff varieties. In particular, Demjén tuff has the highest total porosity and the lowest bulk density (Table 1), statistically affected by the low standard deviation. This is an index of textural uniformity. On the other hand, Bogács tuff is characterized by the lowest total porosity and the highest bulk density. Among the studied tuffs, Sirok shows the highest standard deviation for total and effective porosity (Table 1). The degree of pore interconnection is the highest for Demjén, with an effective porosity of 72.6% of the rock volume, and the lowest for Bogács, with an effective porosity representing only 54% of the total porosity. The high pore volume and interconnection in Demjén tuff is associated with a distinctively higher water absorption and salt penetration, which explains the much lower durability to salt crystallization, especially since pore-size distribution is quite similar to Bogács tuff. In addition, the lower tensile strength implies a poorer mechanical performance when in-pore stresses are generated during salt crystallization and dissolution [23].

Table 1. Average (±standard deviation) values of bulk density, total, and effective porosity estimated on untreated tuff varieties.

Tuff Variety	Total Porosity (%)	Effective Porosity (%)	Bulk Density (g/cm³)
Bogács	29.37 (±2.1)	15.86 (±0.7)	1.78 (±0.05)
Demjén	37.15 (±0.5)	26.97 (±0.4)	1.51 (±0.01)
Sirok	32.93 (±3.7)	22.15 (±2.2)	1.64 (±0.09)

As the salt crystallization tests go on, considerations can be made only on the strongest specimens of Bogács and Sirok, although no relevant differences between the two tuffs can be highlighted as the cycles progress, with the relevant n'_{Hg} and n_{He} porosity values keeping almost constant trends. This can be explained by the progressive salt accumulation within the rock pores, which balances the ongoing rock weathering, hiding its effects on the porosity. This consideration is strengthened by the positive trend of mass change shown in Figure 3.

Moreover, considerations about the possible changes in pore-size distribution as salt weathering progresses can be presented only about Bogács and Sirok tuffs, supported by the full MIP datasets in Supplementary File S1. Bogács tuff shows no significant changes in pore-size distribution, characterized by capillary pores in the approximate range between 1 and 10 μm, which stays virtually the same during the continuation of the tests. Sirok tuff has a higher concentration of micropores, with broader and multimodal pore-size distribution curves, with peaks mainly in the approximate range between 0.01 and 1 μm; no clear trend of changing pore-size distribution during the experimental tests is noticeable, apart from a certain degree of disturbance (i.e., higher pore-size variability) from the 4th salt crystallization cycle onwards in Table 2. However, since the number of capillary pores (those most involved in the mechanisms of water absorption and movement) is lower in Sirok tuff, the prosecution of the salt tests with a higher number of cycles might eventually highlight the higher durability of this material [23].

Table 2. Results of the porosity measurements of the tuff specimens subjected to different numbers of salt crystallization cycles. The full pore-size distributions by MIP are included in Supplementary File S1.

Tuff Variety	Sample ID	Cycle Number	He Pycnometry				MIP		
			Matrix Density (g/cm³)	Bulk Density (g/cm³)	Total Porosity (%)	Specific Pore Volume (cm³/g)	Main Peaks of Pore-Size Distribution Curves (μm)	Open Porosity (%)	Specific Surface Area (m²/g)
Bogács	BG_C_8	4	2.5713 (±0.0003)	1.818 (±0.001)	29.29 (±0.05)	0.161 (±3.5 × 10⁻⁴)	4.99 | 2.88	25.67	10.54
	BG_C_S_19	6	2.5207 (±0.0004)	1.809 (±0.001)	28.22 (±0.02)	0.156 (±1.6 × 10⁻⁴)	4.73 | 3.11	23.80	11.15
	BG_C_09	10	2.5414 (±0.0001)	1.835 (±0.001)	27.79 (±0.04)	0.151 (±3.2 × 10⁻⁴)	4.74 | 2.96 | 0.07	26.29	9.32
	BG_C_11	23	2.5343 (±0.0003)	1.897 (±0.001)	25.13 (±0.04)	0.132 (±2.9 × 10⁻⁴)	5.53 | 4.99	19.81	9.42
Demjén	DJ_S_09	2	2.4977 (±0.0004)	1.474 (±0.002)	40.97 (±0.06)	0.278 (±7.2 × 10⁻⁴)	5.99	31.66	3.38
Sirok	SK_S_07	2	2.4983 (±0.0010)	1.685 (±0.002)	32.57 (±0.10)	0.193 (±8.5 × 10⁻⁴)	12.2 | 0.10	30.42	13.50
	SK_35	4	2.4617 (±0.0004)	1.709 (±0.002)	30.58 (±0.10)	0.179 (±8.2 × 10⁻⁴)	1.04 | 0.08 | 0.02	22.76	15.20
	SK_S_21	6	2.4788 (±0.0005)	1.713 (±0.001)	30.87 (±0.04)	0.180 (±2.8 × 10⁻⁴)	0.14	26.39	10.76
	SK_S_31	10	2.4786 (±0.0009)	1.739 (±0.001)	29.83 (±0.04)	0.172 (±2.5 × 10⁻⁴)	1.04 | 0.02	23.60	15.82
	SK_S_34	23	2.4546 (±0.0009)	1.763 (±0.002)	28.16 (±0.07)	0.160 (±4.8 × 10⁻⁴)	0.13	23.41	12.34

6. Results of IR Cooling Monitoring

The analysis of the thermal images acquired for the untreated tested specimens (Cycle 0) during the cooling monitoring (Figure 2) shows that the rock cooling proceeds towards the inner rock in a generally uniform way, according to literature accounts [21], thanks to the circular geometry of the specimen' face. Thermal images keep a good definition for the entire monitoring time windows, allowing the good identification of the rock face and sampling its average surface temperature (Figure 2).

According to the estimated temperature values and the calculated cooling rates, the untreated specimens of the Demjén variety were characterized by the highest CRIs, suggesting the fastest cooling among the tested groups, followed by Sirok and Bogács (Figure 4a). For all the cases, the standard deviation is low, thus suggesting the reliability of the considered average values. The highest CRIs are referred to as the 5 min time window, when the temperature difference between the specimen and the laboratory environment is maximum. This is in accordance with Newton's law of cooling and previous literature accounts on this test [19]. Therefore, the cooling speed is maximum at the initial stages of the test and tends to slow down as time passes, as shown by the progressively decreasing angle of the cooling curves (Figure 4b). By analyzing the representative cooling curves reported in Figure 4b, it can be stated that the Demjén variety is characterized by the fastest cooling, considering the common initial stage and the lowest surface temperature reached at the end of the monitoring. This trend is more apparent even focusing on the initial segment, used to calculate CRI_5, which is steeper for Demjén, thus suggesting the highest cooling rate within the first 5 min of monitoring. Similarly, the less steep curve is related to the Bogács variety, thus suggesting a lower cooling rate, and supporting the average data reported in Figure 4a.
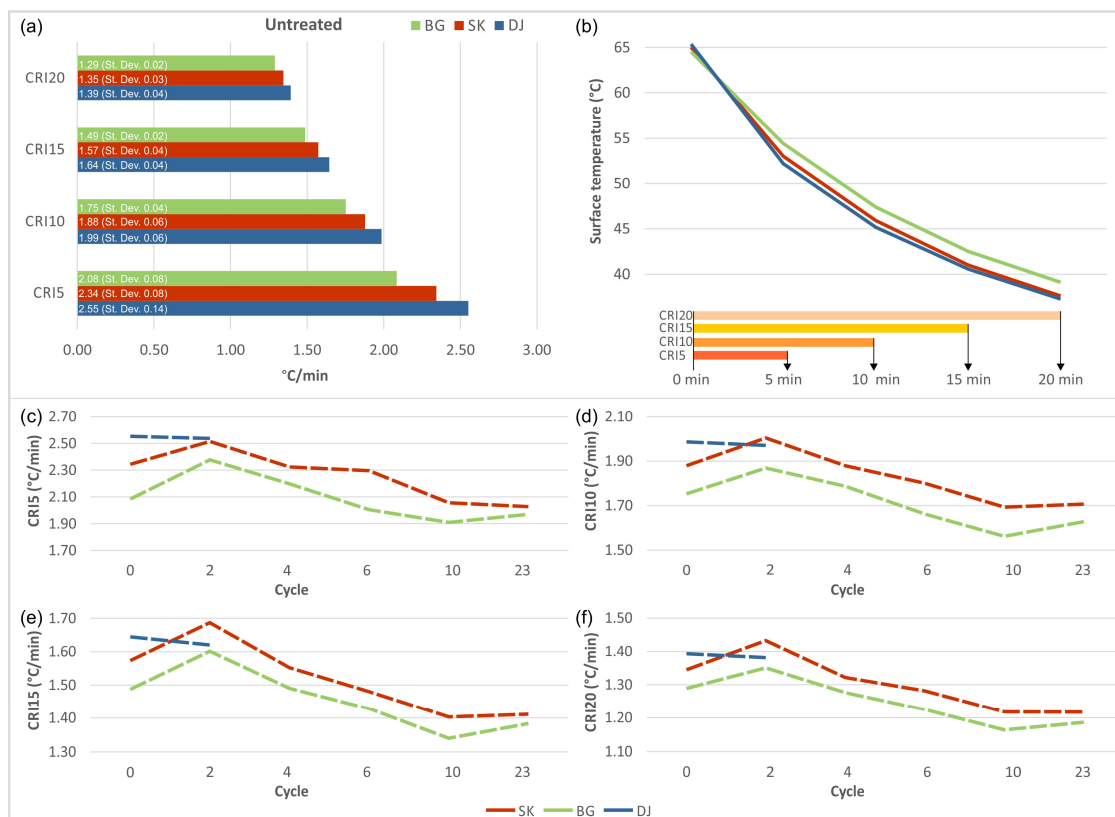

Figure 4. CRI values and cooling curves of tuffs: (**a**) comparison between the average CRI values measured for the three tuff varieties in untreated conditions; (**b**) cooling curves of selected representative untreated specimens belonging to each group; average trends of (**c**) CRI_5, (**d**) CRI_{10}, (**e**) CRI_{15}, and (**f**) CRI_{20} trend with cycle progression. Key: SK—Sirok, BG—Bogács, DJ—Demjén.

By looking at the average CRI trend as the cycles progress (the standard deviation related to each average value is generally <0.1), an initial increase can be reported, with respect to Sirok and Bogács, between Cycle 0 and Cycle 2 (Figure 4c–f). This is about 6%–7% and 5%–12% for Sirok and Bogács, respectively. On the other hand, on average, a CRI decrease of around 1% was found for Demjén (Figure 4c–f). It has to be noted that after the 2nd cycle, no Demjén specimen resisted the crystallization tests, thus the following analysis is referred only to Bogács and Sirok. The related mean CRIs tend to decrease according to an almost constant trend until the 10th cycle. Only the average CRI_5 of Sirok measured between the 4th and the 6th shows a minimal difference (Figure 4c). From the 10th to the 23rd cycle, Sirok's CRIs keep an almost constant value, while Bogács's values mark a slight increase of about 2%–4%.

7. Statistical Correlations

7.1. CRI and Rock Porosity on Untreated (Cycle 0) Specimens

To shed light on the statistical correlation between CRI and rock porosity, experimental cooling data referring to Cycle 0 were plotted against both n and n'_{H_2O} values (Figure 5). Scatter plots show a positive, linear trend between the variables, proving that the fastest rock cooling is related to the most porous rocks. This outcome, verified herein for the tested tuffs' total and effective porosity, is in accordance with literature accounts [19–22].
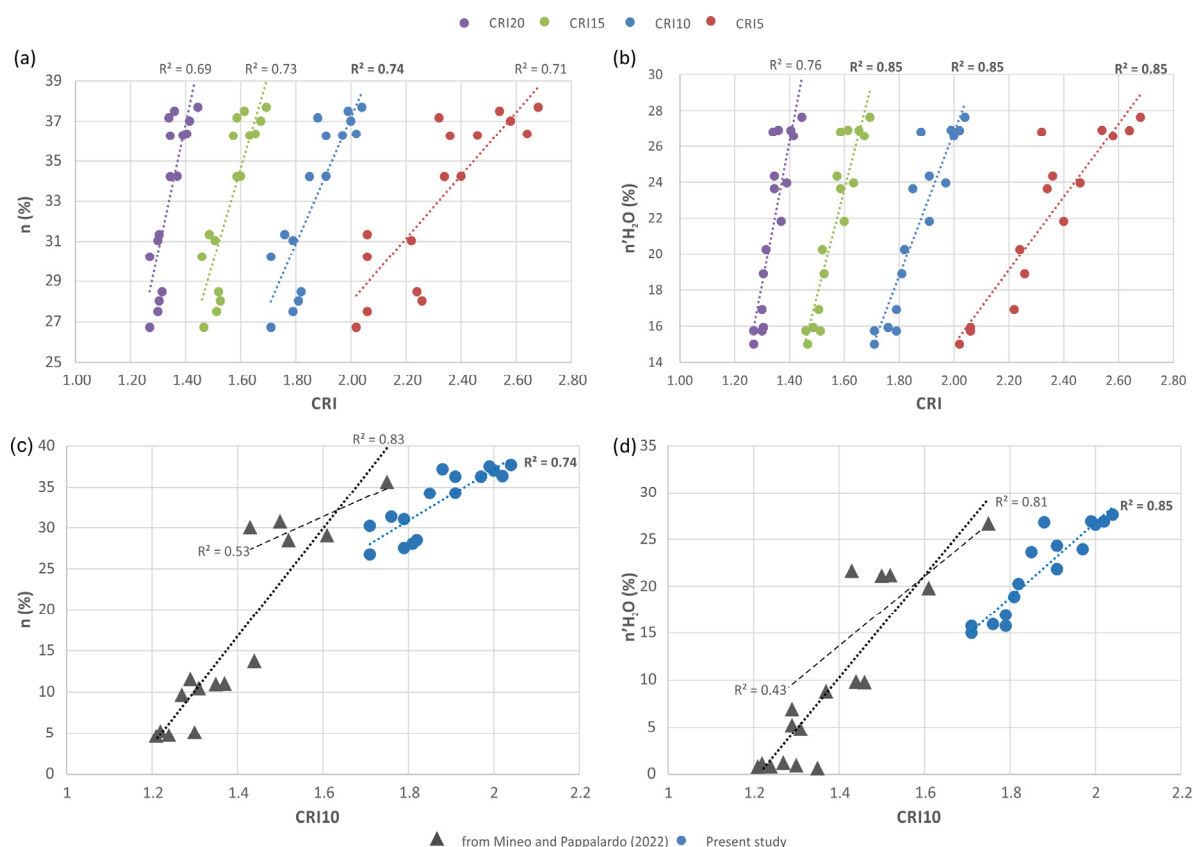
Figure 5. Statistical relationship between thermal cooling and rock porosity for untreated (Cycle 0) specimens: (**a**) correlation diagram CRI vs. total porosity; (**b**) correlation diagram CRI vs. effective porosity; (**c**) CRI_{10} vs. total porosity: comparison between data from this study and literature [21] (dotted lines are the best fit of the whole sets, while the dashed black line is the best fit of literature data involving only specimens with $n > 25\%$ for a more specific comparison); (**d**) CRI_{10} vs. effective porosity: comparison between data from this study and literature [21] (dotted lines are the best fit of the whole sets, while the dashed black line is the best fit of literature data involving only specimens with $n'_{H_2O} \geq 10\%$ for a more specific comparison).

The best correlation of total porosities is achieved by CRI_{10}, with a trend characterized by a 0.74 R^2 against the minimum value of 0.69 belonging to the correlation with CRI_{20} (Figure 5a). On the other hand, the best statistical correlations involving n'_{H_2O} refer to CRI_5, CRI_{10}, and CRI_{15} being characterized by a 0.85 R^2 (Figure 5b). Based on these outcomes, the potential of CRI_{10} for rock porosity prediction is herein strengthened according to Equations (4) and (5). These describe the best trends achieved with the non-standard cylindrical specimens tested for this study, which had a 50 mm diameter and a 30 mm height (indicative volume of 59 cm^3). This is significant, since there is no literature experience on such specimen size. The only available literature data of rock specimens with a somewhat similar size, tested by IRTest, are related to 1:1 small rock cylinders with a 54 mm diameter (indicative volume of 124 cm^3) [21].

It is, therefore, valuable to compare such data to evaluate their scientific soundness. To this purpose, the experimental CRI_{10} statistical plots of the Hungarian tuffs were overlapped with those published in the literature [21] related to the 1:1 small cylinders, bearing in mind the volume difference (Figure 5c,d). It can be noted that the rocks tested herein are, indeed, characterized by a higher cooling rate due to their smaller volume. Nevertheless, a balanced trend comparison should be carried out by taking into account only the specimens showing similar porosity values. Therefore, by focusing the analysis only on the greatest porosity ranges ($n > 25\%$ and $n'_{H_2O} \geq 10\%$), the statistical trends appear sub-parallel, and the highest R^2 values belong to the Hungarian tuffs tested for this study in both n and n'_{H_2O} cases (Figure 5c,d).

$$n\ (\%) = 31.58\ CRI_{10} - 26 \tag{4}$$

$$n'_{H_2O}(\%) = 40.13\ CRI_{10} - 53.45 \tag{5}$$

### 7.2. CRI and Rock Porosity after Salt Crystallization Cycles

Similarly to what was carried out for the fresh samples, a simple regression analysis between CRI and rock porosity was performed to determine if the statistical relationship persists for weathered rocks (Figure 6a,b). In this case, the CRIs calculated for the rocks belonging to Cycle 2 were taken into account. The results show that the statistical trends described by CRI and n fail to equal the previous ones in terms of statistical goodness (Figure 6a). In fact, more scattered plots were achieved, with maximum R^2 values of 0.53. The worst correlation (R^2 0.23) was found for CRI_5, while the best one refers to CRI_{10}. A similar outcome was outlined for n'_{H_2O}, although with slightly higher R^2 values, with particular reference to CRI_{15} (Figure 6b).

Considering the satisfactory correlations related to the untreated specimens, along with the available literature experience, the poor statistical significance achieved in this case casts doubt on the reliability of the procedure used to estimate rock porosity for the weathered specimens. In fact, the buoyancy method requires the specimen immersion in water for at least 24 h, to achieve saturation. This procedure likely affected the measurements in two ways: (1) weathered rocks tend to gain a looser structure, favoring a certain loss of mass during immersion; (2) salt crystals precipitated within the rock pores could likely be involved in dissolution processes when the rock is saturated. Both circumstances lead to possible dissimilarities between wet and dry specimen masses for the porosity calculation, likely making the so-measured porosity values unrepresentative. Therefore, with the aim of looking for a better statistical relation for such non-standard rock specimens, the n'_{Hg} and n_{He} porosity values, estimated on fragments belonging to 10 selected rock specimens (see Section 3.3), were taken into account. These data were plotted against the CRI values, regardless of the salt crystallization cycle (from Cycle 2 to Cycle 23), and the best fit was achieved for the correlations involving CRI_{20} (Figure 6c,d; Equations (6) and (7)).

$$n'_{Hg} = 30\ CRI_{20} - 12.6 \tag{6}$$

$$n_{He} = 36.6\,CRI_{20} - 15.95 \tag{7}$$
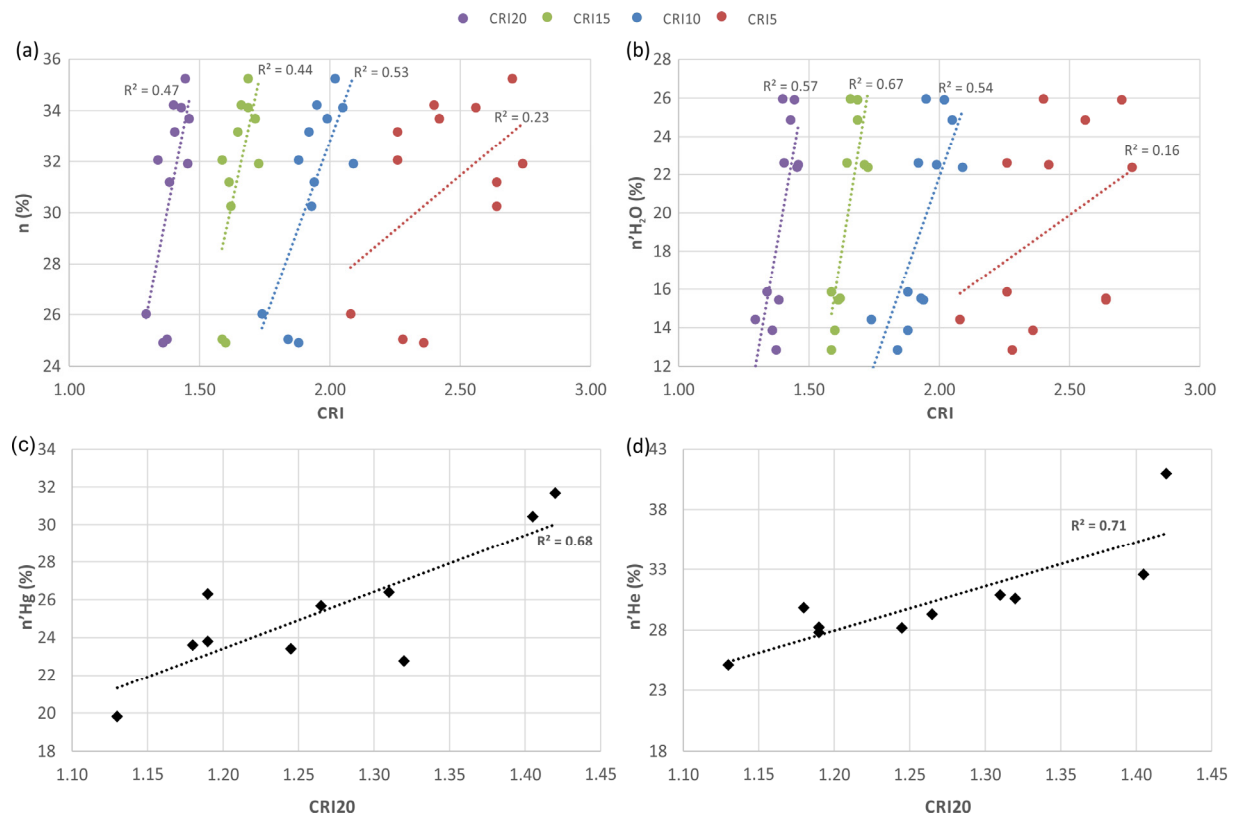
Figure 6. Statistical relationship between thermal cooling and rock total porosity, calculated through the buoyancy method, for the specimens subjected to 2 cycles (**a**); statistical relationship between thermal cooling and rock n'_{H_2O} for the specimens subjected to 2 cycles (**b**); best statistical trend achieved by plotting n'_{Hg} vs. CRI_{20} (**c**); best statistical trend achieved by plotting n_{He} vs. CRI_{20} (**d**).

8. Discussion and Conclusions

The results achieved by this study confirm that the rock cooling process, monitored by IRT through the IRTest, is related to porosity. This is demonstrated by satisfactory linear statistical trends obtained by plotting the rock porosity against the calculated CRIs. It was confirmed that the cooling of rock is directly proportional to the rock volume occupied by voids, concerning both total and effective porosity. In fact, the higher the rock porosity, the faster its cooling. According to the literature background on rock properties and Newton's law of cooling, the cooling velocity of oven-heated rocks is characterized by the highest rates during the first minutes. Then, it tends to slow down as the temperature difference between the rock and the surrounding environment gets smaller. This is confirmed by the trend shown by the cooling curves taken as examples in Figure 4b. The results show also that the cooling rate measured within the first 10 min of cooling (CRI_{10}), which is known in the literature to be a good porosity predictor [19–22], keeps its prediction potential thanks to the best correlations achieved with n and n'_{H_2O}. Its role was strengthened herein by comparing literature data and the experimental results referring to the untreated Hungarian tuffs specimens (Figure 5c,d).

A further consideration is for the specimens' size; in fact, rocks tested for this study had about half of the volume of the specimens from the study taken as Reference [21]. It resulted that the rocks tested herein are characterized by a higher cooling rate due to their smaller volume, underlying that the rock volume plays a key role in the cooling speed, with the highest rates related to lower volumes. Although this study demonstrated that the CRI

works fine also for such small rock specimens, there is the need of referring to standardized sample dimensions in the perspective of the potential standardization of such approaches.

Besides the considerations on the untreated specimens, which are essential to have the IRTest validated even for non-standard-sized rock specimens, interesting discussion points arise from the tests carried out on rocks treated by salt crystallization. From the 2nd to the 23rd cycle, n'_{Hg} and n_{He} were taken as a reference for the pioneering correlation against CRI. Positive linear trends were achieved by considering the 20 min time window (CRI_{20}) for all the selected specimens (Figure 6c,d). This is double the most suitable time window for untreated rocks (10 min) and the reason for that should be searched in the effects that salt crystallization has within the rock texture. This aspect needs to be further investigated, even questioning if an application for the specific IRTest can be posted in terms of crystallization cycles. Figure 4c,f show that CRIs between the 10th and the 23rd cycle remain almost constant for Sirok and are affected by an inverse trend for Bogács. However, the good match between rock cooling and Hg-He porosity suggests that porosity plays a leading role in rock cooling and that IR monitoring is a useful approach for its indirect estimation, even for weathered rocks.

Although needing further experimentation, the application of this method to stone materials used in the Hungarian cultural heritage opens interesting possibilities for the imaging and textural characterization of historical materials. At this stage of development, the technique provides a promising perspective in the frame of stone testing for cultural heritage, although available results refer only to the laboratory setting. Moreover, it is totally non-destructive, since it works with temperatures that do not cause significant changes in structural water content, irreversible strains, or mineralogical transformations. In the frame of technological development, more research is needed to find and set a comparable procedure that could be extended for in situ tests.

Conflicts of Interest: The authors declare no conflict of interest.

References

1. Hatzor, Y.H.; Palchik, V. A Microstructure-Based Failure Criterion for Aminadav Dolomites. *Int. J. Rock Mech. Min. Sci.* **1998**, *35*, 797–805. [CrossRef]
2. Vernik, L.; Bruno, M.; Bovberg, C. Empirical Relations between Compressive Strength and Porosity of Siliciclastic Rocks. *Int. J. Rock Mech. Min. Sci. Geomech. Abstr.* **1993**, *30*, 677–680. [CrossRef]
3. Al-Harthi, A.A.; Al-Amri, R.M.; Shehata, W.M. The Porosity and Engineering Properties of Vesicular Basalt in Saudi Arabia. *Eng. Geol.* **1999**, *54*, 313–320. [CrossRef]

4.   Chang, C.; Zoback, M.D.; Khaksar, A. Empirical Relations between Rock Strength and Physical Properties in Sedimentary Rocks. *J. Pet. Sci. Eng.* **2006**, *51*, 223–237. [CrossRef]

5.   Basu, A.; Celestino, T.B.; Bortolucci, A.A. Evaluation of Rock Mechanical Behaviors under Uniaxial Compression with Reference to Assessed Weathering Grades. *Rock Mech Rock Eng* **2009**, *42*, 73–93. [CrossRef]

6.   Palchik, V. Influence of Porosity and Elastic Modulus on Uniaxial Compressive Strength in Soft Brittle Porous Sandstones. *Rock Mech. Rock Eng.* **1999**, *32*, 303–309. [CrossRef]

7.   Pappalardo, G.; Mineo, S. Static Elastic Modulus of Rocks Predicted through Regression Models and Artificial Neural Network. *Eng. Geol.* **2022**, *308*, 106829. [CrossRef]

8.   Sousa, L.M.O.; Suárez Del Río, L.M.; Calleja, L.; Ruiz De Argandoña, V.G.; Rey, A.R. Influence of Microfractures and Porosity on the Physico-Mechanical Properties and Weathering of Ornamental Granites. *Eng. Geol.* **2005**, *77*, 153–168. [CrossRef]

9.   Thaulow, N.; Sahu, S. Mechanism of Concrete Deterioration Due to Salt Crystallization. *Mater. Charact.* **2004**, *53*, 123–127. [CrossRef]

10. Benavente, D.; Sanchez-Moral, S.; Fernandez-Cortes, A.; Cañaveras, J.C.; Elez, J.; Saiz-Jimenez, C. Salt Damage and Microclimate in the Postumius Tomb, Roman Necropolis of Carmona, Spain. *Environ. Earth Sci.* **2011**, *63*, 1529–1543. [CrossRef]

11. Pappalardo, G.; Mineo, S.; Caliò, D.; Bognandi, A. Evaluation of Natural Stone Weathering in Heritage Building by Infrared Thermography. *Heritage* **2022**, *5*, 2594–2614. [CrossRef]

12. Keppert, M. *Damage of Porous Stones by Salt Crystallization*; Čáchová, M., Fořt, J., Koňáková, D., Pavlík, Z., Černý, R., Eds.; WIT Transactions on Modelling and Simulation; WIT Press: Opatija, Croatia, 2015; pp. 333–341. [CrossRef]

13. Germinario, L.; Oguchi, C.T. Underground Salt Weathering of Heritage Stone: Lithological and Environmental Constraints on the Formation of Sulfate Efflorescences and Crusts. *J. Cult. Herit.* **2021**, *49*, 85–93. [CrossRef]

14. Germinario, L.; Andriani, G.F.; Laviano, R. Decay of Calcareous Building Stone under the Combined Action of Thermoclastism and Cryoclastism: A Laboratory Simulation. *Constr. Build. Mater.* **2015**, *75*, 385–394. [CrossRef]

15. Germinario, L.; Oguchi, C.T. Gypsum, Mirabilite, and Thenardite Efflorescences of Tuff Stone in the Underground Environment. *Environ. Earth Sci.* **2022**, *81*, 242. [CrossRef]

16. Ulusay, R. (Ed.) *The Complete ISRM Suggested Methods for Rock Characterization, Testing and Monitoring: 1974–2006*; Commission on Testing Methods; International Society for Rock Mechanics: Ankara, Turkey, 2007.

17. *EN1936:2006*; European Standard 1936: 2006 Natural Stone Test Methods—Determination of Real Density and Apparent Density, and of Total and Open Porosity. European Union: Maastricht, The Netherlands, 2006.

18. Siegesmund, S.; Durrast, H. Physical and Mechanical Properties of Rocks. In *Stone in Architecture. Properties, Durability*, 5th ed.; Siegesmund, S., Snethlage, R., Eds.; Springer: Berlin, Germany, 2014; pp. 97–224.

19. Mineo, S.; Pappalardo, G. The Use of Infrared Thermography for Porosity Assessment of Intact Rock. *Rock Mech. Rock Eng.* **2016**, *49*, 3027–3039. [CrossRef]

20. Mineo, S.; Pappalardo, G. InfraRed Thermography Presented as an Innovative and Non-Destructive Solution to Quantify Rock Porosity in Laboratory. *Int. J. Rock Mech. Min. Sci.* **2019**, *115*, 99–110. [CrossRef]

21. Mineo, S.; Pappalardo, G. Nondestructive Rock Porosity Estimation by InfraRed Thermography Applied to Natural Stones. *Constr. Build. Mater.* **2022**, *342*, 127950. [CrossRef]

22. Mineo, S.; Pappalardo, G. Preliminary Results on the Estimation of Porosity in Intact Rock through InfraRed Thermography. *ROL* **2016**, *41*, 317–320. [CrossRef]

23. Germinario, L.; Török, Á. Variability of Technical Properties and Durability in Volcanic Tuffs from the Same Quarry Region— Examples from Northern Hungary. *Eng. Geol.* **2019**, *262*, 105319. [CrossRef]

24. Germinario, L.; Török, Á. Surface Weathering of Tuffs: Compositional and Microstructural Changes in the Building Stones of the Medieval Castles of Hungary. *Minerals* **2020**, *10*, 376. [CrossRef]

25. Lukács, R.; Harangi, S.; Guillong, M.; Bachmann, O.; Fodor, L.; Buret, Y.; Dunkl, I.; Sliwinski, J.; Von Quadt, A.; Peytcheva, I.; et al. Early to Mid-Miocene Syn-Extensional Massive Silicic Volcanism in the Pannonian Basin (East-Central Europe): Eruption Chronology, Correlation Potential and Geodynamic Implications. *Earth-Sci. Rev.* **2018**, *179*, 1–19. [CrossRef]

26. DeWitt, D.P.; Nutter, G.D. *Theory and Practice of Radiation Thermometry*; Wiley: New York, NY, USA, 1988.

27. Thomachot-Schneider, C.; Gommeaux, M.; Lelarge, N.; Conreux, A.; Mouhoubi, K.; Bodnar, J.-L.; Vázquez, P. Relationship between Na_2SO_4 Concentration and Thermal Response of Reconstituted Stone in the Laboratory and on Site. *Environ. Earth Sci.* **2016**, *75*, 762. [CrossRef]

28. Thomachot-Schneider, C.; Vázquez, P.; Gommeaux, M.; Lelarge, N.; Conreux, A.; Drothière, X.; Mouhoubi, K.; Bodnar, J.-L. Thermal Response of Building Stones Contaminated with Salts. *Constr. Build. Mater.* **2019**, *226*, 331–344. [CrossRef]

29. Vazquez, P.; Thomachot-Schneider, C. Infrared Thermography as a Tool to Detect Increasing Cracking in Granitic Stones Exposed to High Temperatures. *J. Cult. Herit.* **2023**, *59*, 163–170. [CrossRef]

30. Franzosi, F.; Casiraghi, S.; Colombo, R.; Crippa, C.; Agliardi, F. Quantitative Evaluation of the Fracturing State of Crystalline Rocks Using Infrared Thermography. *Rock Mech. Rock Eng.* **2023**. [CrossRef]

31. Caliò, D.; Mineo, S.; Pappalardo, G. Digital Rock Mass Analysis for the Evaluation of Rockfall Magnitude at Poorly Accessible Cliffs. *Remote Sens.* **2023**, *15*, 1515. [CrossRef]

32. Mineo, S.; Caliò, D.; Pappalardo, G. UAV-Based Photogrammetry and Infrared Thermography Applied to Rock Mass Survey for Geomechanical Purposes. *Remote Sens.* **2022**, *14*, 473. [CrossRef]

33. Frodella, W.; Elashvili, M.; Spizzichino, D.; Gigli, G.; Adikashvili, L.; Vacheishvili, N.; Kirkitadze, G.; Nadaraia, A.; Margottini, C.; Casagli, N. Combining InfraRed Thermography and UAV Digital Photogrammetry for the Protection and Conservation of Rupestrian Cultural Heritage Sites in Georgia: A Methodological Application. *Remote Sens.* **2020**, *12*, 892. [CrossRef]

34. Pappalardo, G.; Mineo, S.; Carbone, S.; Monaco, C.; Catalano, D.; Signorello, G. Preliminary Recognition of Geohazards at the Natural Reserve "Lachea Islet and Cyclop Rocks" (Southern Italy). *Sustainability* **2021**, *13*, 1082. [CrossRef]

35. Guerin, A.; Jaboyedoff, M.; Collins, B.D.; Derron, M.-H.; Stock, G.M.; Matasci, B.; Boesiger, M.; Lefeuvre, C.; Podladchikov, Y.Y. Detection of Rock Bridges by Infrared Thermal Imaging and Modeling. *Sci. Rep.* **2019**, *9*, 13138. [CrossRef]

36. Grechi, G.; Fiorucci, M.; Marmoni, G.M.; Martino, S. 3D Thermal Monitoring of Jointed Rock Masses through Infrared Thermography and Photogrammetry. *Remote Sens.* **2021**, *13*, 957. [CrossRef]

37. Mineo, S.; Pappalardo, G. Rock Emissivity Measurement for Infrared Thermography Engineering Geological Applications. *Appl. Sci.* **2021**, *11*, 3773. [CrossRef]

38. Hall, C.; Hamilton, A. Porosities of Building Limestones: Using the Solid Density to Assess Data Quality. *Mater. Struct.* **2016**, *49*, 3969–3979. [CrossRef]